


# Shadow and observational images of the rotating Hayward black hole with thin disk accretion

Zheng-Xue Chang(常正雪), Shu-Min Wang(王树民), Chen-Yu Yang(杨晨昱), Yu-Bin Wang(王榆斌), and Ke-Jian He(何柯腱)

**Citation:**Chin. Phys. B, 2026, 35 (**6**): 069701. DOI: 10.1088/1674-1056/ae29fa
http://cpb.iphy.ac.cn; http://iopscience.iop.org/cpb

**What follows is a list of articles you may be interested in**

---

## Resonant behavior of stochastic oscillations of general relativistic disks driven by a memory-damped friction

Wang Zhi-Yun (汪志云), Chen Pei-Jie (陈培杰), Zhang Liang-Ying (张良英)
Chin. Phys. B, 2015, 24 (**5**): 059801. DOI: 10.1088/1674-1056/24/5/059801

## Quantum nonthermal radiation and horizon surface gravity of an arbitrarily accelerating black hole with electric charge and magnetic charge

Xie Zhi-Kun (谢志堃), Pan Wei-Zhen (潘伟珍), Yang Xue-Jun (杨学军)
Chin. Phys. B, 2013, 22 (**3**): 039701. DOI: 10.1088/1674-1056/22/3/039701

## Jet precession in neutrino-cooled disks for gamma-ray bursts: The effects of the mass and spin of a black hole

Liu Tong(刘彤) and Xue Li(薛力)
Chin. Phys. B, 2012, 21 (**6**): 069801. DOI: 10.1088/1674-1056/21/6/069801

---

# Shadow and observational images of the rotating Hayward black hole with thin disk accretion

Zheng-Xue Chang(常正雪)[1,†], Shu-Min Wang(王树民)[1,‡], Chen-Yu Yang(杨晨昱)[2,§], Yu-Bin Wang(王榆斌)[3,¶], and Ke-Jian He(何柯腱)[2,*]

[1] *College of Mathematics and Physics, Handan University, Handan* 056005, *China*
[2] *Department of Mechanics, Chongqing Jiaotong University, Chongqing* 400000, *China*
[3] *School of Physics and Electronic Engineering, Sichuan University of Science & Engineering, Zigong* 643000, *China*

(Received 28 August 2025; revised manuscript received 16 November 2025; accepted manuscript online 9 December 2025)

We investigate the shadow and observational characteristics of rotating Hayward black holes by employing a ray-tracing method combined with stereographic projection. By solving the photon geodesics derived from the Hamilton–Jacobi equation, we explore how the spin parameter $a$ and magnetic charge $g$ influence the shape of the black hole shadow and its observable optical properties. The results indicate that an increase in the spin parameter $a$ leads to a pronounced D-shaped deformation of the shadow, whereas higher values of the magnetic charge $g$ significantly reduce the size of its inner region. When a thin accretion disk surrounds the black hole, variations in $a$ and $g$ directly affect observable features, including the size of the inner shadow and the intensity of the emitted radiation. Furthermore, the direct and lensed images exhibit distinct redshift features, highlighting the strong sensitivity of gravitational lensing effects to the parameters $a$ and $g$. These findings suggest that rotating Hayward black holes can be distinguished from Kerr black holes through their observable characteristics, thereby providing a valuable reference for testing alternative theories of gravity.

**Keywords:** shadow, observer characteristuc, rotating black hole

**PACS:** 97.60.Lf, 97.10.Gz, 98.62.Sb

**DOI:** 10.1088/1674-1056/ae29fa **CSTR:** 32038.14.CPB.ae29fa

## 1. Introduction

The Event Horizon Telescope (EHT) collaboration has successfully captured the first images of the central regions of M87* and Sgr A*,[1,2] revealing a dark central silhouette surrounded by a bright emission ring. The dark interior corresponds to the black hole shadow, while the surrounding bright structure is commonly referred to as the photon ring. The formation of the shadow arises due to the extreme curvature of spacetime near the event horizon, which bends the paths of photons and prevents them from reaching distant observers.[3,4] More precisely, photons approaching the black hole are deflected by its gravitational field, leading to a critical boundary delineated by unstable photon orbits, which defines the apparent shadow observed at infinity.

Understanding black hole shadows has emerged as a fundamental endeavor in contemporary black hole physics, as the geometry of the shadow encodes crucial information about the black hole's physical parameters, such as its mass, spin, and electromagnetic charge. Furthermore, shadow analysis offers a valuable window into the nature of accretion processes, relativistic jet dynamics, and emission mechanisms operating in strong-gravity environments. It also serves as a promising tool to probe the validity of general relativity and its possible extensions. For example, while a non-rotating Schwarzschild black hole produces a perfectly circular shadow, a rapidly spinning Kerr black hole exhibits a characteristic "D"-shaped shadow due to frame-dragging effects.[5] In addition, extensive studies within modified gravity frameworks have revealed novel features in shadow structures, such as the presence of secondary shadows or additional photon rings, which provide powerful constraints on alternative theories through precise astronomical measurements.[6–20]

On the other hand, Cunha *et al.*[21] introduced a four-color celestial sphere light source model to simulate Einstein rings and black hole shadow images, thereby providing a novel visual representation of photon trajectories in the vicinity of black holes. This modeling framework has since been extended to black holes within various modified gravity theories.[22] In realistic astrophysical settings, black holes are not isolated objects but are typically surrounded by complex accretion environments.[23] For instance, in the case of a Schwarzschild black hole enveloped by a static, optically thin, spherically symmetric accretion medium, the influence of the accreting matter on the shadow is minimal.[24] However, when

[†]Corresponding author. E-mail: changzx520@163.com
[‡]Corresponding author. E-mail: wangshumin@hdc.edu.cn
[§]Corresponding author. E-mail: chenyuyang2024@163.com
[¶]Corresponding author. E-mail: wangyubin@suse.edu.cn
[*]Corresponding author. E-mail: kjhe94@163.com

© 2026 Chinese Physical Society and IOP Publishing Ltd. All rights, including for text and data mining, AI training, and similar technologies, are reserved.

the black hole is instead surrounded by a geometrically and optically thin disk aligned with the equatorial plane, the resulting image – especially from a near-polar observer's viewpoint – exhibits a prominent shadow encircled by a multi-layered emission ring, composed of direct emission, lensing rings, and photon rings.[25]

Building on this, recent research has adopted similar disk models to analyze black hole shadows across a wide variety of spacetime geometries, including those involving non-Einsteinian compact objects. These investigations have yielded a wealth of theoretical insights into the formation, deformation, and energy distribution of observed shadows.[26–43] In a related study, Hou *et al.* examined how factors such as black hole spin, magnetic fields, and the observer's inclination angle affect the resulting shadow and image morphology of a Kerr–Melvin black hole with a thin accretion disk,[44] in which the plasma disk moves along Keplerian orbits outside the innermost stable circular orbit (ISCO) and follows precessing geodesics inside the ISCO. Simultaneously, substantial advances have been made in the imaging of hotspots, accretion disk modeling, and associated shadow phenomena.[45–60]

In this study, we investigate the observational signatures of rotating Hayward black holes illuminated by a thin accretion disk. Due to the influence of magnetohydrodynamic processes in the vicinity of black holes, studies involving black hole imaging must be grounded in general relativistic magnetohydrodynamics (GRMHD).[61] However, substantial challenges arise in solving the GRMHD equations and implementing numerical simulations. As a result, developing simplified accretion models is essential for investigating the optical observational characteristics of black holes. Theoretically, such simplified models are often adequate for capturing the fundamental features of black hole images and have therefore been extensively studied, including spherical accretion and thin disk accretion models.[62–71] Furthermore, the Hayward solution, recognized as a prominent regular (nonsingular) black hole solution, has garnered significant scholarly attention. To circumvent classical singularities, Bardeen initially proposed a regular black hole configuration,[72] while Ayon-Beato and collaborators showed that the Bardeen black hole can be interpreted as a solution sourced by a nonlinear magnetic monopole.[73–76] Hayward black holes were subsequently introduced in Ref. [77], and their critical thermodynamic phenomena have been extensively studied, particularly in anti-de Sitter (AdS) spacetimes.[78] By leveraging recent advancements in black hole imaging techniques, this study employs a thin accretion disk model to systematically analyze the shadow structures, inner shadows, celestial sphere images, and illumination patterns of accretion disks associated with rotating Hayward black holes. We focus on how variations in the relevant parameters affect the optical observational features of Hayward black holes. This comprehensive analysis provides distinct observational criteria for clearly distinguishing rotating Hayward black holes from Kerr black holes through high-resolution astronomical observations.

This paper is organized as follows. In Section 2, we systematically investigate the shadow geometry, including its size, shape, and asymmetry. Section 3 presents detailed analyses of celestial sphere images surrounding the black hole. We then explore images derived from thin accretion disk models. Finally, Section 4 summarizes our key findings and discusses the implications for future observational tests.

## 2. Shadows of the rotating Hayward black hole

In Boyer–Lindquist coordinates, the metric of the rotating Hayward black hole can be represented as[77]

$$\begin{aligned} \mathrm{d}s^2 =& -\left(1-\frac{2\mathcal{M}(r)r}{\Sigma}\right)\mathrm{d}t^2 - \frac{4a\mathcal{M}(r)r\sin^2\theta}{\Sigma}\mathrm{d}t\,\mathrm{d}\phi \\ &+\frac{\Sigma}{\Delta}\mathrm{d}r^2+\Sigma\,\mathrm{d}\theta^2 \\ &+\left(r^2+a^2+\frac{2a^2\mathcal{M}(r)r\sin^2\theta}{\Sigma}\right)\sin^2\theta\,\mathrm{d}\phi^2, \end{aligned} \tag{1}$$

where

$$\begin{aligned} &\Sigma = r^2+a^2\cos^2\theta,\ \ \Delta = r^2-2\mathcal{M}(r)r+a^2, \\ &\mathcal{M}(r) = M\frac{r^3}{r^3+g^3}. \end{aligned} \tag{2}$$

In the above equation, $a$ is the spin parameter and $g$ is the magnetic charge. The metric takes the form of a Kerr black hole with mass $\mathcal{M}(r)$, where $\mathcal{M}(r)$ represents the total mass contained within the region defined by the constant radial coordinate $r$. In the limit as $r\to\infty$, $\mathcal{M}(r)$ converges to the black hole mass parameter $M$, that is, $\lim_{r\to\infty}\mathcal{M}(r)=M$. In addition, the location of the event horizon is determined by setting $\Delta=0$. One can investigate the photon geodesics to analyze the shadow cast by this nonsingular rotating black hole. To proceed, we first observe that, for a particle of mass $m$, the canonical Hamiltonian is given by

$$H=\frac{1}{2}g^{\mu\nu}p_\mu p_\nu=-\frac{1}{2}m^2, \tag{3}$$

where $p_\mu$ denotes the four-momentum of the particle. Utilizing spacetime symmetries and associated Killing vectors, we obtain two conserved quantities along each geodesic: the energy $E$ and the angular momentum $L$, given by

$$\begin{aligned} E &= -p_t = -g_{\phi t}\frac{\mathrm{d}\phi}{\mathrm{d}\tau}-g_{tt}\frac{\mathrm{d}t}{\mathrm{d}\tau}, \\ L &= p_\phi = g_{\phi\phi}\frac{\mathrm{d}\phi}{\mathrm{d}\tau}+g_{\phi t}\frac{\mathrm{d}t}{\mathrm{d}\tau}, \end{aligned} \tag{4}$$

with affine parameter $\tau$. For null geodesics ($m=0$) around the rotating Hayward black hole, the photon equations of motion derived from Eq. (4) are expressed as follows:

$$\Sigma\frac{\mathrm{d}t}{\mathrm{d}\tau}=a\left(L_z-Ea\sin^2\theta\right)+\frac{r^2+a^2}{\Delta}\left[(r^2+a^2)E-aL_z\right], \quad (5)$$

$$\Sigma\frac{\mathrm{d}\phi}{\mathrm{d}\tau}=\left(\frac{L_z}{\sin^2\theta}-aE\right)+\frac{a}{\Delta}\left[(r^2+a^2)E-aL_z\right], \quad (6)$$

$$\Sigma\frac{\mathrm{d}r}{\mathrm{d}\tau}=\pm\sqrt{\mathcal{R}}, \quad (7)$$

$$\Sigma\frac{\mathrm{d}\theta}{\mathrm{d}\tau}=\pm\sqrt{\Theta}, \quad (8)$$

with

$$\mathcal{R}=\left[(r^2+a^2)E-aL_z\right]^2-\Delta\left[\mathcal{K}+(L_z-aE)^2\right], \quad (9)$$

$$\Theta=\mathcal{K}+\cos^2\theta\left(a^2E^2-\frac{L_z^2}{\sin^2\theta}\right). \quad (10)$$

Here, the symbol $\mathcal{K}$ denotes the Carter constant. Unstable circular photon orbits satisfy

$$\mathcal{R}(r)=0,\quad \frac{\mathrm{d}\mathcal{R}(r)}{\mathrm{d}r}=0. \quad (11)$$

Hence, it follows

$$r^4+\left(a^2-\xi^2-\eta\right)r^2+2m\left[\eta+(\xi-a)^2\right]r-a^2\eta=0, \quad (12)$$

$$4r^3+2\left(a^2-\xi^2-\eta\right)r+2m\left[\eta+(\xi-a)^2\right]-2m'\left[\eta+(\xi-a)^2\right]r=0, \quad (13)$$

where the parameters $\xi$ and $\eta$ read as

$$\xi=\left.\frac{m\left(a^2-3r^2\right)+r(r^2+a^2)\left(m'+1\right)}{a\left[m+r(m'-1)\right]}\right|_{r=r_\mathrm{p}}, \quad (14)$$

$$\eta=-\frac{r^3}{a^2}\left.\left[(1+m'^2)r^3+2m'\left(r^2-3mr+2a^2\right)r-m\left(6r^2-9mr+4a^2\right)\right]\left[m+r(m'-1)\right]^{-2}\right|_{r=r_\mathrm{p}}. \quad (15)$$

Here, $m'$ denotes $\mathrm{d}m/\mathrm{d}r$, and $r_\mathrm{p}$ represent the radius of the unstable circular photon orbits. By imposing the requirement $\Theta\geq 0$, the photon region condition is derived as

$$\eta-\xi^2\cot^2\theta\geq -a^2\cos^2\theta. \quad (16)$$

Considering the time-translation and axial symmetries, a zero-angular-momentum observer (ZAMO) at infinity, with coordinates $\left(0,r_\mathrm{o},\theta_\mathrm{o},0\right)$, has an orthonormal tetrad

$$e_0=e_{(t)}=\zeta\partial_t+\gamma\partial_\phi,\ \ e_1=-e_{(r)}=-\frac{\partial r}{\sqrt{g_{rr}}},$$
$$e_2=e_{(\theta)}=\frac{\partial\theta}{\sqrt{g_{\theta\theta}}},\ \ e_3=-e_{(\phi)}=-\frac{\partial\phi}{\sqrt{g_{\phi\phi}}}, \quad (17)$$

where

$$\zeta=\sqrt{\frac{-g_{\phi\phi}}{g_{tt}g_{\phi\phi}-g_{t\phi}^2}},\ \ \gamma=-\frac{g_{t\phi}}{g_{\phi\phi}}\sqrt{\frac{-g_{\phi\phi}}{g_{tt}g_{\phi\phi}-g_{t\phi}^2}}. \quad (18)$$

Here, $e_0$ is the timelike vector, essentially the observer's four-velocity, and $e_1$ points toward the black hole center. With this ZAMO tetrad, one can use stereographic projection to visualize how the black hole shadow and images are formed, as depicted in Fig. 1. The observer is located at point $O$ (with coordinates $(r_O,\theta_O)$), and the red geodesic starting at $O$ has tangent $\boldsymbol{OP}$ in the observer's local frame. A sphere is drawn with center $O$ and radius $\boldsymbol{OP}$, and the origin of tetrad (5) is placed at $O'$. The line $O'S$ through $O$ serves as the sphere's diameter and aligns with $e_1$. A rectangular screen through $O'$ (shaded in blue) displays the resultant black hole shadow and image. By projecting $\boldsymbol{OP}$ onto the screen, one obtains the vector $\boldsymbol{O'P'}$. To specify the photon's angular location, we define celestial coordinates $(\alpha,\beta)$, where $\alpha$ is the angle between $OO'$ and $OP$, and $\beta$ is the angle between $OQ$ and $e_2$. If $s(\tau)=\left(t(\tau),r(\tau),\theta(\tau),\phi(\tau)\right)$ represents a null geodesic, then its tangent vector can be expressed as a linear combination of the tetrad basis vectors $e_i$ $(i=0,1,2,3)$, that is

$$\begin{aligned}\dot{s}&=\dot{r}\,\partial_r+\dot{\theta}\,\partial_\theta+\dot{\phi}\,\partial_\phi+\dot{t}\,\partial_t\\&=|\boldsymbol{OP}|\left(-\chi e_0+\cos\alpha\,e_1+\sin\alpha\cos\beta\,e_2+\sin\alpha\sin\beta\,e_3\right).\end{aligned} \quad (19)$$

Since the photon's trajectory does not depend on its energy, we set the photon's energy in the camera frame to unity. It can be written as

$$E_\mathrm{camera}=1=|\boldsymbol{OP}|\cdot\chi=-\left.\frac{E}{\sqrt{g_{tt}}}\right|_{(r_O,\theta_O)}. \quad (20)$$

In the ZAMO frame, the photon's four-momentum reads

$$p_{(\mu)}=p_\nu e^\nu_{(\mu)}. \quad (21)$$

Then, the relation between the photon's four-momentum $p_{(\mu)}$ and the celestial coordinates is Ref. [79]

$$\cos\alpha=\frac{p^{(1)}}{p^{(0)}},\ \ \tan\beta=\frac{p^{(3)}}{p^{(2)}}. \quad (22)$$

Hence, in the rotating Hayward black hole, the celestial angles $\alpha$ and $\beta$ become

$$\alpha=\arccos\left\{\frac{\sqrt{\mathcal{M}+\mathcal{A}^2\left(\Delta-a^2\sin^2\theta\right)}}{\sqrt{\Delta}\left(a^2\cos^2\theta+\mathcal{H}\right)\left[\mathcal{A}-a\,\xi(r_\mathrm{p})\left(\mathcal{H}-\mathcal{F}\mathcal{H}\right)\right]}\times\sqrt{\mathcal{N}-2a\mathcal{H}(1-\mathcal{F})\,\xi(r_\mathrm{p})-\mathcal{F}\mathcal{H}\,\xi(r_\mathrm{p})^2-\Delta\,\eta(r_\mathrm{p})}\right\}, \quad (23)$$

$$\beta=\arctan\left[\frac{\xi(r_\mathrm{p})\left(a^2\cos^2\theta+\mathcal{H}\right)}{\sqrt{\mathcal{A}\sin^2\theta}\sqrt{a^2\cos^2\theta+\eta(r_\mathrm{p})-\cot^2\theta\,\xi(r_\mathrm{p})^2}}\right]. \quad (24)$$

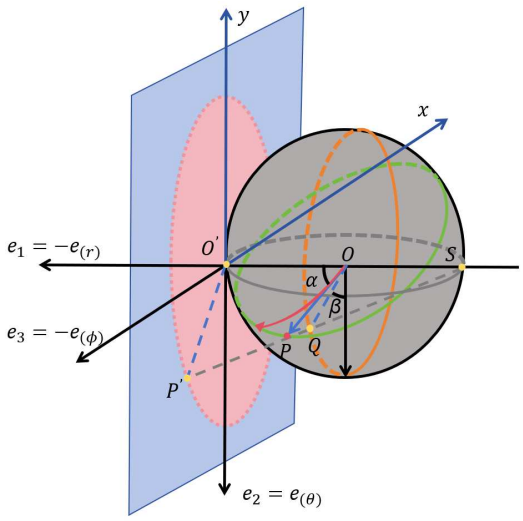



**Fig. 1.** The orthonormal tetrad for a ZAMO and the celestial coordinates $(\alpha,\beta)$ with stereographic projection.

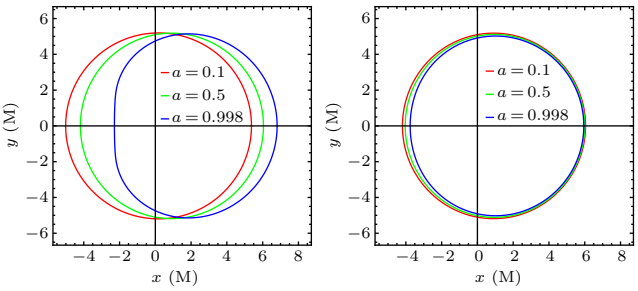



**Fig. 2.** The shadows corresponding to various rotation parameters $a$ and magnetic charges $g$ are presented. Panel (a) displays the circular photon orbits for $a = 0.1, 0.5, 0.998$, represented by dashed, solid, and dotted lines, respectively, with the magnetic charge fixed at $g = 0.1$. Panel (b) shows the circular photon orbits for magnetic charges $g = 0.01, 0.7, 0.9$, indicated by dashed, solid, and dotted lines, respectively, with the rotation parameter fixed at $a = 0.5$. In both scenarios, the black hole mass is set as $M = 1$, and the angle is fixed at $\theta = 65°$.

Finally, we define the Cartesian coordinates $(x,y)$ on the rectangular screen in Fig. 1, and one can get that

$$x = -2\tan\left(\frac{\alpha}{2}\right)\sin\beta, \quad y = -2\tan\left(\frac{\alpha}{2}\right)\cos\beta. \tag{25}$$

Using Eq. (25), one can visualize the black hole's shadow on the screen and thus examine how the rotation parameter $a$ and the magnetic charge $g$ affect its shape. In Fig. 2, we analyze the shape and size of shadows corresponding to varying values of the rotation parameter $a$ and the magnetic charge $g$. The left panel illustrates the circular orbits for different spin parameters $a$, demonstrating that as $a$ increases, the circular orbits shift toward the positive $x$-axis, resulting in more pronounced shadow deformation. In the right panel, the shadow size slightly decreases and shifts marginally towards the positive $x$-axis with increasing magnetic charge $g$. When $g = 0.01$, the shadow appears nearly perfectly circular. In subsequent sections, we will further investigate these visual differences, highlighting their potential as observational signatures to distinguish rotating Hayward black holes from Kerr black holes.

## 3. Images illuminated by the thin accretion disk

Now we adopt the backward ray-tracing method to investigate the images of rotating black holes in greater detail. Following the celestial light source setup, the black hole is placed at the center of the celestial sphere, and due to its comparatively negligible size and the large distance between the observer and the origin, we take the black hole's rotation axis to align with the North Pole. We also assume that the observer resides in the equatorial plane of the sphere. In this construction, the celestial sphere is partitioned into four quadrants: the green quadrant, defined by $0 \le \theta \le \pi/2$ and $0 \le \phi \le \pi$; the red quadrant, satisfying $0 \le \theta \le \pi/2$ and $\pi \le \phi \le 2\pi$; the blue quadrant, characterized by $\pi/2 \le \theta \le \pi$ and $0 \le \phi \le \pi$; and the yellow quadrant, corresponding to $\pi/2 \le \theta \le \pi$ and $\pi \le \phi \le 2\pi$. We generate the black hole images by applying the numerical method described in Ref. [79]. First, the fisheye camera model is used to project the photon momentum $p_\mu$ onto the screen via stereographic projection; then, we solve the null geodesics originating from the observer by integrating their equations of motion. In Hamiltonian form, these equations are given by

$$\dot{x}^\mu = \frac{\partial H}{\partial p_\mu}, \quad \dot{p}_\mu = -\frac{\partial H}{\partial x^\mu}. \tag{26}$$

By means of Eq. (26), we determine the color of the location at which each light ray intersects the celestial sphere. Any rays reaching the event horizon are assigned a black color. Figure 3 displays the black hole shadow regions in the four-color celestial sphere model for different rotation parameters $a$ and magnetic charges $g$. Here, the field of view denotes the camera's viewing angle, and the observer is positioned at $(r_O, \theta_O)$. When the rotation parameter is fixed at $a = 0.05$, the shadow maintains a circular shape. However, as $a$ increases, the shadow area takes on a more pronounced "D" configuration. Under variation of the magnetic charge $g$, the changes in the shadow boundary are comparatively subtle.

Next, we investigate the images of the rotating Hayward black hole surrounded by a thin accretion disk following the approach outlined in Ref. [44]. We assume that the observer is sufficiently far from the black hole and that the accretion disk, lying in the equatorial plane, is both geometrically and optically thin, as illustrated in Fig. 4. The innermost stable circular orbit (ISCO) naturally partitions the disk into two regions: a stable circular orbit beyond the ISCO and an infalling flow within the ISCO. The light rays interacting with the accretion disk may intersect it once, twice, or multiple times. We label the first intersection at radius $r_1$ as the direct image, while a second intersection at radius $r_2$ gives rise to the lensed image.

Since the disk extends from the event horizon $r_\mathrm{h}$ up to a distant outer boundary $r_\mathrm{f} = 10000$, we restrict the observer to satisfy $r_+ \ll r_O < r_\mathrm{f}$. For the rotating Hayward black hole, the ISCO location can be obtained by solving

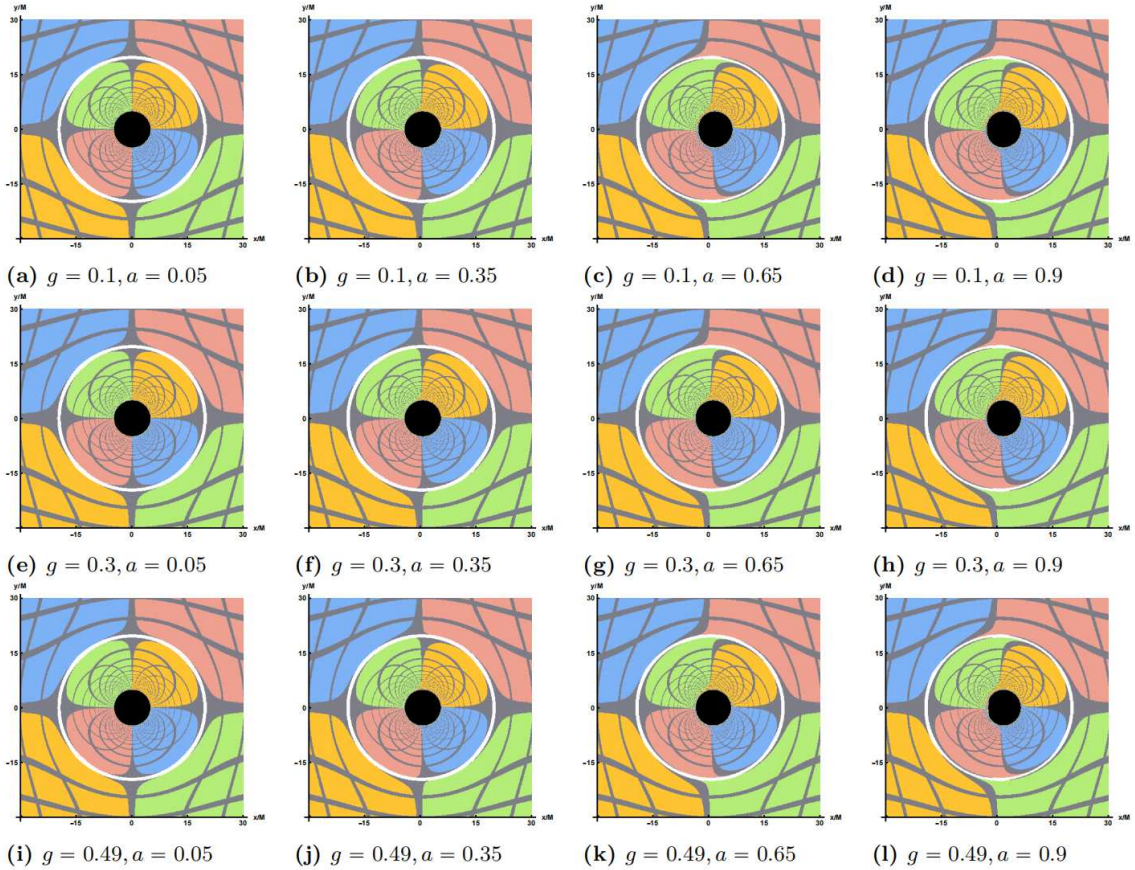



**Fig. 3.** Under illumination by the four-color celestial sphere model, we present shadow images produced by rotating Hayward black holes for different values of the rotation parameter $a$ and the magnetic charge $g$. In all cases, the observer is positioned at $r_{\rm obs} = 100$, the field of view is set to 35°, and the angle is fixed at $\theta = 76°$.

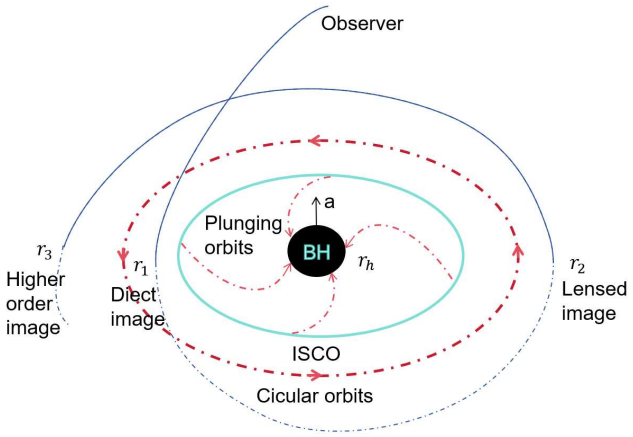



**Fig. 4.** Imaging the rotating Hayward black hole with a thin accretion disk.

$$V_{\rm eff}\big|_{r=r_{\rm ISCO}} = 0, \quad \partial_r V_{\rm eff}\big|_{r=r_{\rm ISCO}} = 0, \quad \partial_r^2 V_{\rm eff}\big|_{r=r_{\rm ISCO}} = 0, \tag{27}$$

where $V_{\rm eff}$ denotes the effective potential. Furthermore, for a massive particle with four-velocity $u^a$, we have

$$V_{\rm eff}(r,\tilde{E},\tilde{L}) = \left[1 + g^{tt}\tilde{E}^2 + g^{\phi\phi}\tilde{L}^2 - 2g^{t\phi} \quad \tilde{E} \quad \tilde{L}\right]\Big|_{\theta=\pi/2}. \tag{28}$$

Here, $\tilde{E}$ and $\tilde{L}$ represent the specific energy and angular momentum of the particle, which is

$$\tilde{E} = -\frac{g_{tt} + g_{t\phi}\,\Omega}{\sqrt{-g_{tt} - 2\,g_{t\phi}\,\Omega - g_{\phi\phi}\,\Omega^2}}, \tag{29}$$

where

$$\Omega = \frac{{\rm d}\phi}{{\rm d}t} = \frac{\partial_r g_{t\phi} + \sqrt{\partial_r^2 g_{t\phi} - (\partial_r g_{tt})(\partial_r g_{\phi\phi})}}{\partial_r g_{\phi\phi}}. \tag{30}$$

Let $\tilde{E}_{\rm ISCO}$ and $\tilde{L}_{\rm ISCO}$ be the energy and angular momentum of the accretion flow on the ISCO. For material flowing outside the ISCO, the four-velocity takes the form

$$u^{\mu}_{\rm out} = \sqrt{\frac{1}{-g_{tt} - 2\,g_{t\phi}\,\Omega - g_{\phi\phi}\,\Omega^2}}\,(1,0,0,\Omega)\big|_{\theta=\pi/2}. \tag{31}$$

Inside the ISCO, the flow plunges radially inward while preserving its constants of motion $\tilde{E}_{\rm ISCO}$ and $\tilde{L}_{\rm ISCO}$. Its four-velocity then becomes

$$u^t_{\rm in} = \left(-g^{tt}\,\tilde{E}_{\rm ISCO} + g^{t\phi}\,\tilde{L}_{\rm ISCO}\right)\Big|_{\theta=\pi/2}, \tag{32}$$

$$u^r_{\rm in} = -\sqrt{-\frac{g_{tt}\,(u^t_{\rm in})^2 + 2\,g_{t\phi}\,u^t_{\rm in}\,u^{\phi}_{\rm in} + g_{\phi\phi}\,(u^{\phi}_{\rm in})^2 + 1}{g_{rr}}}\Bigg|_{\theta=\pi/2}, \tag{33}$$

$$u^{\theta}_{\rm in} = 0, \tag{34}$$

$$u^{\phi}_{\rm in} = \left(-g^{t\phi}\,\tilde{E}_{\rm ISCO} + g^{\phi\phi}\,\tilde{L}_{\rm ISCO}\right)\Big|_{\theta=\pi/2}, \tag{35}$$

for $r_+ < r < r_{\rm ISCO}$. When a light ray intersects the accretion disk, we record its radial coordinate as $r_n$. The observed intensity on the screen is then

$$I_{\nu_{\rm o}} = \sum_{n=1}^{N} f_n g_n^3 J_n(r), \tag{36}$$

where $N$ is the total number of intersections between the ray and the disk, and $f_n = 1$. The factor $g_n = \nu_{\rm o}/\nu_n$ is the redshift, with $\nu_{\rm o}$ and $\nu_n$ being the frequencies measured by the screen and local rest frames, respectively. Considering that the black hole image obtained by the EHT was observed at a wavelength of 1.3 mm (230 GHz), one can adopt the following emissivity profile for the disk

$$J(r) = \exp\left[-\tfrac{1}{2}z^2 - 2z\right], \quad z = \ln\left(\frac{r}{r_+}\right), \tag{37}$$

which is a second-order polynomial in log-space. It should be emphasized that Eq. (36) uses the third power of the redshift shadow $g_n$, which aligns with the intensity measured at the particular frequency of 230 GHz.[80] In contrast, Gralla[81] provided a detailed discussion on the use of the fourth power of the redshift factor $g_n$. Assuming that the accretion disk is a neutral plasma with specific energy $\tilde{E}$ and angular momentum $\tilde{L}$, the redshift factor for the ISCO fluid outside the ISCO is

$$g_n^{\rm out} = \left.\frac{\xi\left(1-\gamma\frac{p_\phi}{p_t}\right)}{\zeta\left(1+\Omega\frac{p_\phi}{p_t}\right)}\right|_{r=r_n}, \quad r > r_{\rm ISCO}, \tag{38}$$

where

$$\gamma = \frac{g_{t\phi}}{g_{\phi\phi}}, \quad \xi = \sqrt{\frac{-g_{\phi\phi}}{g_{tt}\,g_{\phi\phi} - g_{t\phi}^2}},$$
$$\zeta = \sqrt{\frac{-1}{g_{tt} + 2\,g_{t\phi}\,\Omega + g_{\phi\phi}\,\Omega^2}}. \tag{39}$$

The ratio of the observed energy on the screen to the energy along the null geodesic is

$$e = \frac{p_{(t)}}{p_t} = \xi\left(1 - \gamma\frac{p_\phi}{p_t}\right). \tag{40}$$

For an observer at asymptotic infinity in a flat spacetime, $e$ is set to 1. For the infalling flow inside the ISCO, whose radial velocity is $u^r_{\rm in}$, the corresponding redshift factor is

$$g_n^{\rm in} = \left[u^r_{\rm in}\frac{p_r}{p_t} - \tilde{E}_{\rm ISCO}\left(g^{tt} - g^{t\phi}\frac{p_\phi}{p_t}\right) + \tilde{L}_{\rm ISCO}\left(g^{\phi\phi}\frac{p_\phi}{p_t} + g^{t\phi}\right)\right]^{-1}\Bigg|_{r=r_n}, \quad r < r_{\rm ISCO}. \tag{41}$$

In Fig. 5, we present images of the rotating Hayward black hole illuminated by a prograde accretion flow under various rotation parameters $a$ and magnetic charges $g$, observed at a fixed angle $\theta_{\rm obs} = 55°$. Both direct emission

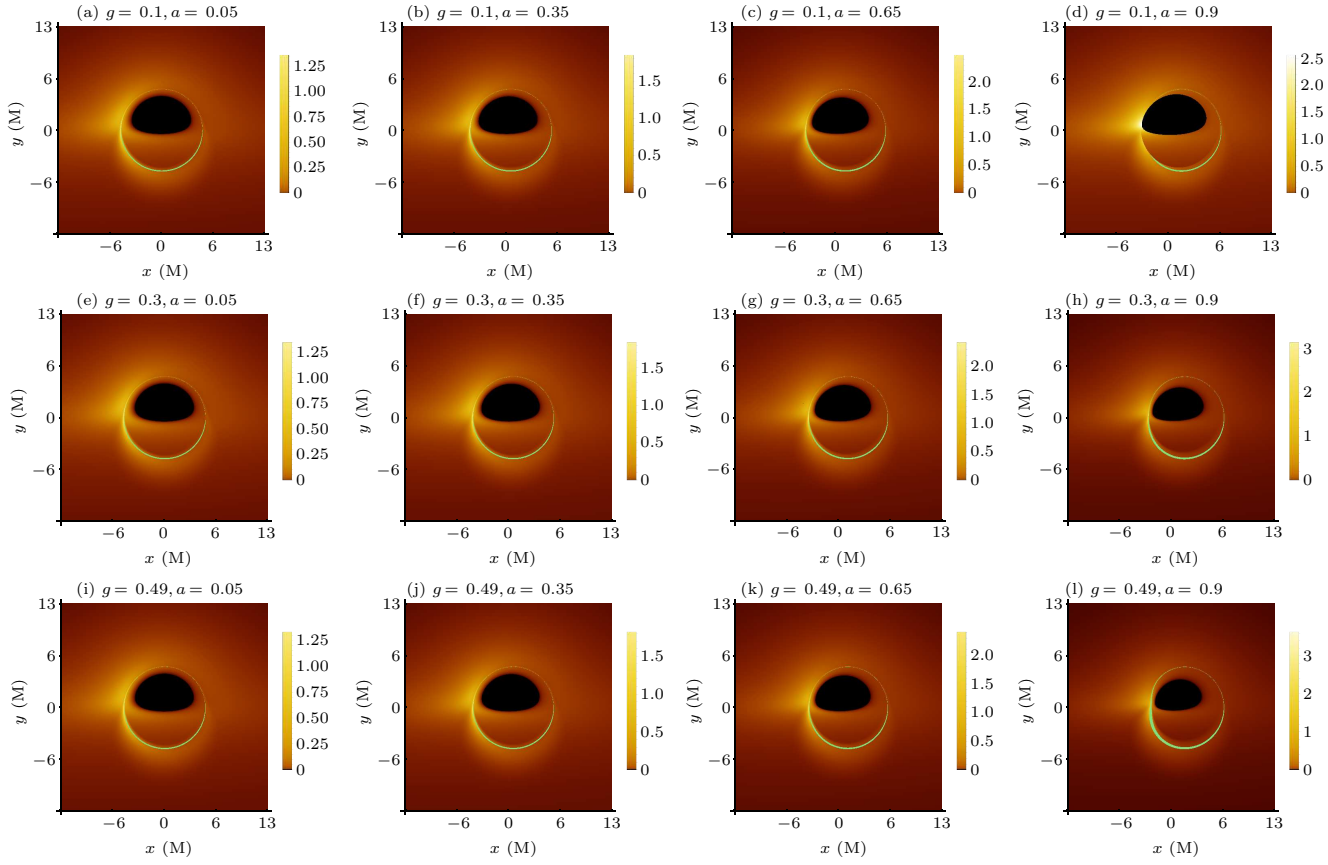
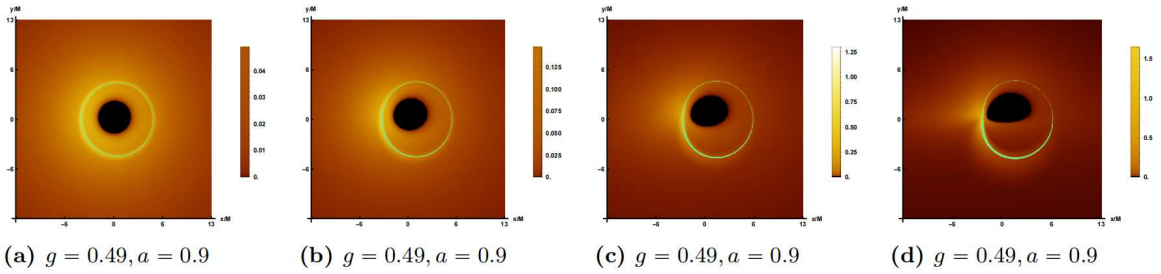



**Fig. 5.** The images of rotating Hayward black holes illuminated by the prograde flows. In all cases, the observer is positioned at $r_{\rm obs} = 100$, the field of view is set to 15°, and the angle is fixed at $\theta = 76°$.



**(a)** $g = 0.49, a = 0.9$ **(b)** $g = 0.49, a = 0.9$ **(c)** $g = 0.49, a = 0.9$ **(d)** $g = 0.49, a = 0.9$

**Fig. 6.** The images depict rotating Hayward black holes illuminated by prograde accretion flows at different observation angles. From left to right, the angles are set as $\theta = 15°, 35°, 55°, 75°$. In all scenarios, the observer is located at $r_{\rm obs} = 100$, and the field of view is fixed at 15°.

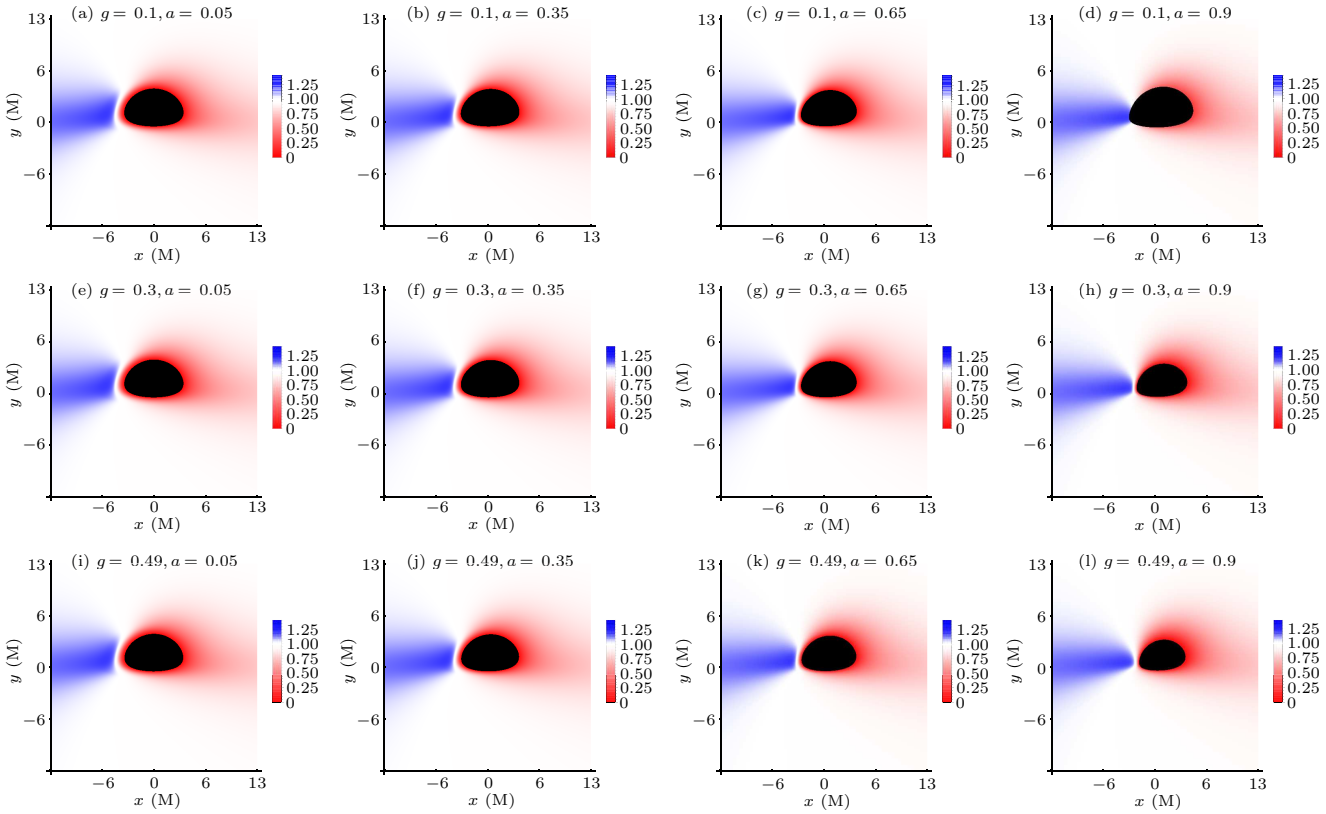
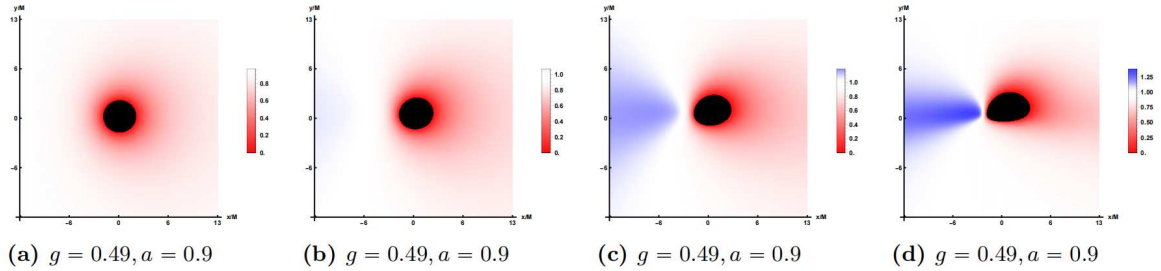



**Fig. 7.** The redshift maps of direct emission from the accretion disk are presented for various rotation parameters $a$ and magnetic charges $g$, with the observer of $\theta_{\rm obs} = 55°$. In all scenarios, the observer is located at $r_{\rm obs} = 100$, with the field of view consistently set at 15°.



**(a)** $g = 0.49, a = 0.9$ **(b)** $g = 0.49, a = 0.9$ **(c)** $g = 0.49, a = 0.9$ **(d)** $g = 0.49, a = 0.9$

**Fig. 8.** The redshift maps of direct emission from the accretion disk are presented for various observation angles $\theta_{\rm obs} \in \{15°, 35°, 55°, 75°\}$, with the rotation parameters $a = 0.49$ and magnetic charges $g = 0.9$. In all scenarios, the observer is located at $r_{\rm obs} = 100$, with the field of view consistently set at 15°.

and gravitationally lensed images are visible, providing insights into the complex interplay between rotation, magnetic charge, and gravitational lensing effects. Specifically, when $g = 0.1$ and the rotation parameter $a$ increases from 0.05 to 0.9, the inner shadow progressively shrinks and transforms into a smaller, semicircular dark region. This transformation vividly illustrates how rotation influences the observational appearance of the black hole shadow. Similar shrinking behavior is observed for increased values of $a$ at higher magnetic charges, such as $g = 0.3$ and $g = 0.49$. Additionally, with a fixed rotation parameter of $a = 0.9$, increasing the magnetic charge to $g = 0.49$ leads to a notably smaller inner shadow compared to

lower values $g = 0.1$ or $g = 0.3$. This distinct feature highlights the potential observational signatures that could differentiate a rotating Hayward black hole from the classical Kerr black hole.

Furthermore, Fig. 6 presents additional visualizations of the black hole at varying observer angles $\theta_{\rm obs} = 15°$, $35°$, $55°$, and $75°$, with rotation and magnetic charge parameters set at $a = 0.9$ and $g = 0.49$, respectively. These images reveal that as the observer's inclination angle increases, the inner shadow progressively evolves into a distinctly semicircular shape. Concurrently, the outer gravitationally lensed image takes on a pronounced "D" shape, further emphasizing the intricate dependence of shadow morphology on observer orientation. Such angle-dependent observational effects underscore the importance of viewing angle in analyzing astrophysical black hole systems.

In Fig. 7, we present the redshift maps of the direct image of the accretion disk for an observer inclination angle $\theta_{\rm obs} = 55°$, exploring various rotation parameters $a$ and magnetic charges $g$. These redshift maps effectively illustrate how gravitational and relativistic effects influence observational features. Taking $g = 0.49$ as a specific example, we observe a distinct trend where increasing the rotation parameter $a$ results in a noticeable reduction of both the inner shadow and the region exhibiting pronounced redshift. Conversely, when $a$ is fixed within the set $\{0.05, 0.35, 0.65, 0.9\}$, varying $g$ produces relatively subtle changes, leaving the size of the inner shadow mostly unaffected. However, an exceptional case occurs when $a = 0.9$ and $g = 0.49$, clearly demonstrating a significant shrinkage of the inner shadow. Such detailed visual analyses underscore the complex interplay between rotation and magnetic charge parameters, further emphasizing their role in shaping observational characteristics of rotating Hayward black holes. Table 1 provides the maximum redshift for distinct values of $a$ and $g$, showing a decreasing trend as $a$ and $g$ grow, which implies that higher magnetic charges reduce the inner shadow's size.

**Table 1.** The maximal redshift under different values of the rotation parameter $a$ and the magnetic charge $g$, respectively. We set $r_b = 1$.

| $g$ \ $a$ | 0.05 | 0.35 | 0.65 | 0.9 |
|---|---|---|---|---|
| 0.1 | 1.02433 | 1.02115 | 1.01112 | 1.00159 |
| 0.3 | 1.02464 | 1.02174 | 1.00784 | 1 |
| 0.49 | 1.0255 | 1.01658 | 1.00821 | 1 |

Figure 8 illustrates redshifted images of the direct disk emission for different observer inclination angles $\theta_{\rm obs} \in \{15°, 35°, 55°, 75°\}$. As the observer angle $\theta_{\rm obs}$ progressively increases, the redshift distribution undergoes noticeable variations, highlighting the significant influence of viewing geometry on observational characteristics. Particularly at the highest inclination angle $\theta_{\rm obs} = 75°$, the inner shadow region exhibits

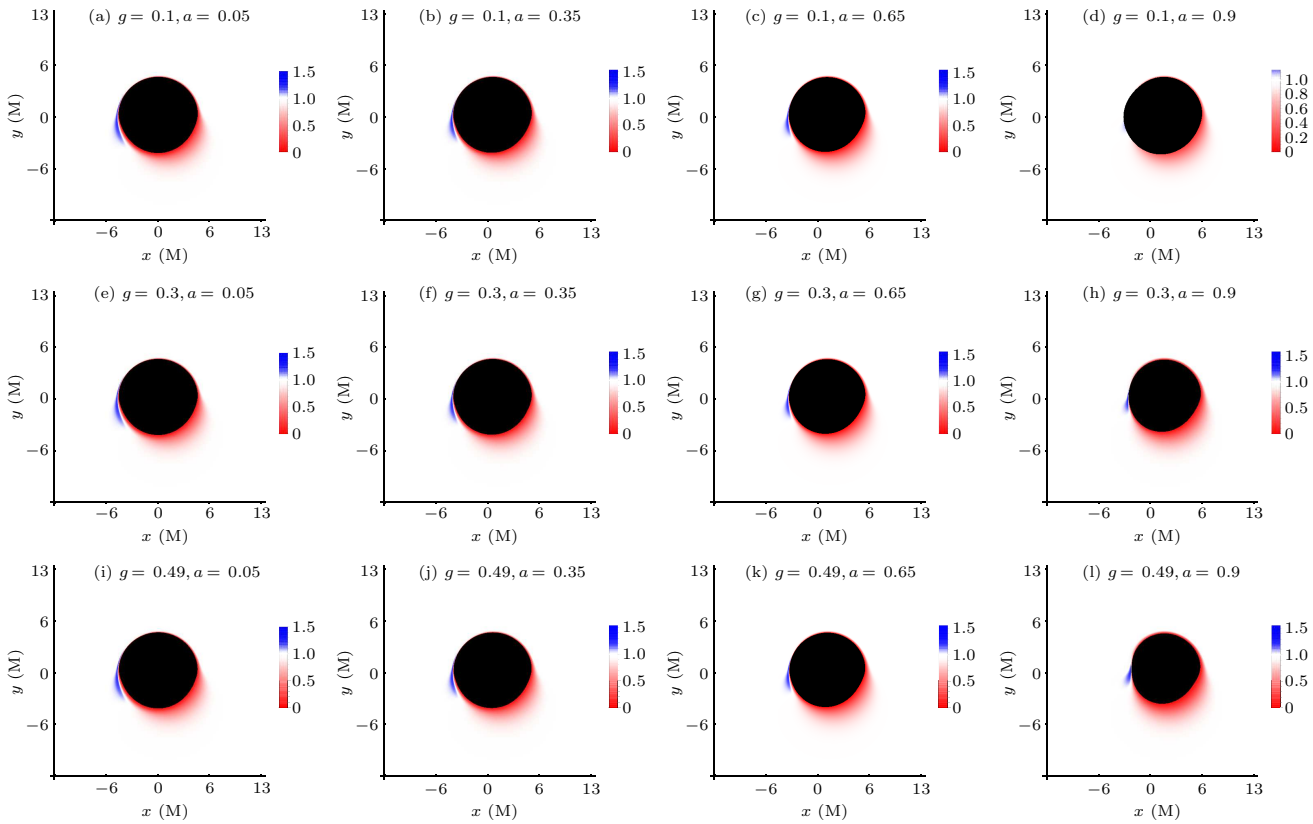
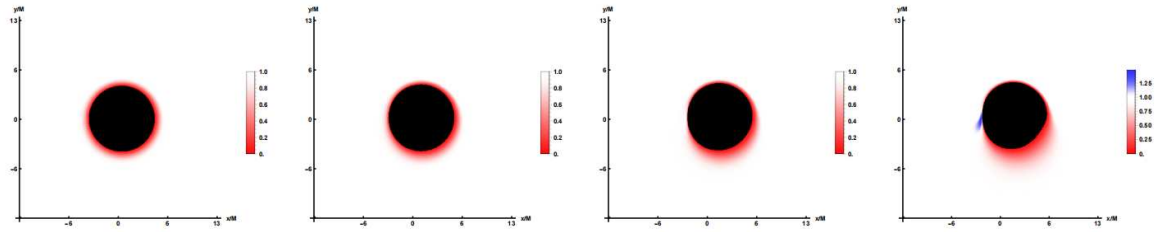



**Fig. 9.** The redshift maps of lensed emission from the accretion disk are presented for various rotation parameters $a$ and magnetic charges $g$, with the observer of $\theta_{\rm obs} = 55°$. In all scenarios, the observer is located at $r_{\rm obs} = 100$, with the field of view consistently set at 15°.



(a) $g = 0.49, a = 0.9$ (b) $g = 0.49, a = 0.9$ (c) $g = 0.49, a = 0.9$ (d) $g = 0.49, a = 0.9$

**Fig. 10.** The redshift maps of lensed emission from the accretion disk are presented for various observation angles $\theta_{\rm obs} \in \{15°, 35°, 55°, 75°\}$, with the rotation parameters $a = 0.49$ and magnetic charges $g = 0.9$. In all scenarios, the observer is located at $r_{\rm obs} = 100$, with the field of view consistently set at 15°.

a distinctly irregular morphology. Such angle-dependent variations further underscore the complex nature of gravitational and relativistic effects shaping the observable features of rotating Hayward black holes.

Moreover, Fig. 9 presents the redshift maps of the lensed images of the accretion disk at a fixed observer inclination of $\theta_{\rm obs} = 55°$, for different values of the rotation parameter $a$ and magnetic charge $g$. Unlike the direct emission maps, the lensed images display more intricate and less predictable redshift structures, with no clear monotonic dependence on increasing $a$ or $g$. This complexity reflects the multifaceted gravitational lensing effects that dominate these regions. Additionally, Fig. 10 displays the redshift maps of lensed images at various inclination angles $\theta_{\rm obs} \in \{15°, 35°, 55°, 75°\}$. As $\theta_{\rm obs}$ increases, the redshifted structures evolve accordingly, and at $\theta_{\rm obs} = 75°$, the inner shadow becomes significantly distorted, exhibiting a highly irregular and asymmetric contour. These findings reinforce the sensitivity of black hole imaging to both intrinsic parameters and viewing orientation.

## 4. Discussion and conclusion

In this work, we have employed a comprehensive ray-tracing framework to analyze the shadow and observational characteristics of the rotating Hayward black hole. Through numerical simulations, we explored its inner shadow structure, celestial sphere imaging, and emission profiles generated by a geometrically thin accretion disk. Utilizing photon geodesics derived from the Hamilton-Jacobi formalism and stereographic projection in the ZAMO reference frame, we examined in detail the effects of the rotation parameter $a$ and magnetic charge $g$ on the appearance of the black hole.

As demonstrated in Fig. 2, when $g = 0.1$ is held fixed, increasing $a$ enhances the distortion of the black hole shadow, manifesting as a clear deviation from circular symmetry. Conversely, fixing $a = 0.5$ and varying $g$ also leads to noticeable changes in the shadow's shape, although the response is more nuanced. In the celestial sphere images shown in Fig. 3, we find that a small rotation (e.g., $a = 0.05$) yields an almost circular shadow, while higher spin induces a distinct "D"-shaped silhouette. Variations in $g$ primarily result in subtle modulations to the shadow boundary. Figures 5 and 6 further reveal that, when illuminated by a prograde accretion flow, the rotating Hayward black hole exhibits a progressively deformed inner shadow with increasing $a$, and that larger values of $g$ tend to shrink the inner shadow region. These patterns serve as observational signatures that may distinguish rotating Hayward black holes from classical Kerr black holes in high-resolution imaging data. In Figs. 7 and 8, we presented redshift maps of the direct disk emission. These maps indicate that both $a$ and $g$ strongly influence redshift distributions and emission morphology. Specifically, Table 1. shows that the maximum redshift values decrease with increasing $a$ and $g$, suggesting that stronger rotation and higher magnetic charge reduce both the size of the inner shadow and the intensity contrast within the disk image. However, the redshift profiles in the lensed images (Figs. 9 and 10) do not exhibit a simple trend, revealing the complexity of gravitational lensing and photon trajectories in curved spacetimes.

Taken together, these findings emphasize the intricate dependencies of shadow morphology and emission characteristics on the parameters $a$ and $g$. Moreover, we demonstrated that increasing the observer inclination angle $\theta_{\rm obs}$ introduces additional distortions, especially in the lensed region, where the outer silhouette acquires a pronounced "D"-like form. As high-resolution observations — such as those from the Event Horizon Telescope — continue to improve, the diagnostic power of shadow imaging will become increasingly valuable. Our results suggest that it is feasible, at least in principle, to constrain the values of $a$ and $g$ based on shadow shape and emission patterns, thereby offering a concrete avenue to differentiate rotating Hayward black holes from other compact objects predicted by general relativity and beyond.

## Acknowledgments

Project supported by the National Natural Science Foundation of China (Grant No. 12303027) , the Natural Science Foundation of Hebei Province (Grant No. A2022109001), and the Sichuan Provincial Natural Science Foundation Project (Grant No. 2025ZNSFSC0878).

## References


[1] Akiyama K, Alberdi A, Alef W, *et al.* 2019 *Astrophys. J. Lett.* **875** L1
[2] Akiyama K, Alberdi A, Alef W, *et al.* 2022 *Astrophys. J. Lett.* **930** L12
[3] Cunha P V P and Herdeiro C A R 2018 *Gen. Relativ. Gravit.* **50** 42
[4] Perlick V and Tsupko O Y 2022 *Phys. Rep.* **947** 1
[5] Chandrasekhar S 1992 *The Mathematical Theory of Black Holes* (New York: Oxford University Press)
[6] Wei S W and Liu Y X 2013 *JCAP* **11** 063
[7] Wei S W, Cheng P, Zhong Y and Zhou X N 2015 *JCAP* **08** 004
[8] Huang Y, Chen S and Jing J 2016 *Eur. Phys. J. C* **76** 594
[9] Cunha P V P, Herdeiro C A R and Radu E 2017 *Phys. Rev. D* **96** 024039
[10] Wang M, Chen S and Jing J 2017 *JCAP* **10** 051
[11] Guo M and Li P C 2020 *Eur. Phys. J. C* **80** 588
[12] Atamurotov F, Abdujabbarov A and Ahmedov B 2013 *Phys. Rev. D* **88** 064004
[13] Perlick V, Tsupko O Y and Bisnovatyi-Kogan G S 2015 *Phys. Rev. D* **92** 104031
[14] Konoplya R A 2019 *Phys. Lett. B* **795** 1
[15] Shaikh R, Kocherlakota P, Narayan R and Joshi P S 2019 *Mon. Not. R. Astron. Soc.* **482** 52
[16] Abdujabbarov A, Amir M, Ahmedov B and Ghosh S G 2016 *Phys. Rev. D* **93** 104004
[17] Amarilla L and Eiroa E F 2012 *Phys. Rev. D* **85** 064019
[18] Nedkova P G, Tinchev V K and Yazadjiev S S 2013 *Phys. Rev. D* **88** 124019
[19] Papnoi U, Atamurotov F, Ghosh S G and Ahmedov B 2014 *Phys. Rev. D* **90** 024073
[20] Meng Y, Kuang X M, Wang X J and Wu J P 2023 *Phys. Lett. B* **841** 137940
[21] Cunha P V P, Herdeiro C A R, Radu E and Runarsson H F 2015 *Phys. Rev. Lett.* **115** 211102
[22] Chen S, Jing J, Qian W L and Wang B 2023 *Sci. China Phys. Mech. Astron.* **66** 260401
[23] Luminet J P 1979 *Astron. Astrophys.* **75** 228
[24] Narayan R, Johnson M D and Gammie C F 2019 *Astrophys. J. Lett.* **885** L33
[25] Gralla S E, Holz D E and Wald R M 2019 *Phys. Rev. D* **100** 024018
[26] Zeng X X and Zhang H Q 2020 *Eur. Phys. J. C* **80** 1058
[27] Li G P and He K J 2021 *JCAP* **06** 037
[28] Zeng X X, He K J and Li G P 2022 *Sci. China Phys. Mech. Astron.* **65** 290411
[29] Zeng X X, Li G P and He K J 2022 *Nucl. Phys. B* **974** 115639
[30] He K J, Li G P, Yang C Y and Zeng X X 2025 *Eur. Phys. J. C* **85** 662
[31] Li G P and He K J 2021 *Eur. Phys. J. C* **81** 1018
[32] Peng J, Guo M and Feng X H 2021 *Chin. Phys. C* **45** 085103
[33] Peng J, Guo M and Feng X H 2021 *Phys. Rev. D* **104** 124010
[34] Zhang C, Ma Y and Yang J 2023 *Phys. Rev. D* **108** 104004
[35] Meng Y, Kuang X M, Wang X J, Wang B and Wu J P 2024 *Eur. Phys. J. C* **84** 305
[36] Luo Z, Li J, He K J and Yu H 2025 *Phys. Lett. B* **871** 139985
[37] Luo Z, Yu H and Li J 2024 *Phys. Rev. D* **109** 104006
[38] Meng Y, Kuang X M, Wang X J, Wang B and Wu J P 2023 *Phys. Rev. D* **108** 064013
[39] Gan Q, Wang P, Wu H and Yang H 2021 *Phys. Rev. D* **104** 044049
[40] Rosa J L, Garcia P, Vincent F H and Cardoso V 2022 *Phys. Rev. D* **106** 044031
[41] Asuküla H, Hohmann M, Karanasou V, Bahamonde S, Pfeifer C and Rosa J L 2024 *Phys. Rev. D* **109** 064027
[42] Rosa J L and Rubiera-Garcia D 2022 *Phys. Rev. D* **106** 084004
[43] Rosa J L, Pelle J and Pérez D 2024 *Phys. Rev. D* **110** 084068
[44] Hou Y, Zhang Z, Yan H, Guo M and Chen B 2022 *Phys. Rev. D* **106** 064058
[45] Huang J, Zhang Z, Guo M and Chen B 2024 *Phys. Rev. D* **109** 124062
[46] Chen Y, Wang P, Wu H and Yang H 2024 *JCAP* **04** 032
[47] Lee T C, Hu Z, Guo M and Chen B 2023 *Phys. Rev. D* **108** 024008
[48] Qin X, Chen S, Zhang Z and Jing J 2022 *Astrophys. J.* **938** 2
[49] Chen Y, Cheng L, Wang P and Yang H 2025 *Phys. Rev. D* **112** 024044
[50] Zhang Z, Hou Y, Guo M and Chen B 2024 *JCAP* **05** 032
[51] Rosa J L, Macedo C F B and Rubiera-Garcia D 2023 *Phys. Rev. D* **108** 044021
[52] He K J, Yang C Y and Zeng X X 2025 arXiv:2501.06778 [astro-ph.HE]
[53] He K J, Ye H, Zeng X X, Li L F and Xu P 2025 *Chin. Phys. B* **49** 125103
[54] Vincent F H, Gralla S E, Lupsasca A and Wielgus M 2022 *Astron. Astrophys.* **667** A170
[55] Zhang M, Pan Q C and Li H L 2025 *Phys. Lett. B* **868** 139782
[56] Övgün A and Fathi M 2025 *Nucl. Phys. B* **1018** 117063
[57] Wang X, Zhao Z, Zeng X X and Wang X Y 2025 *Phys. Rev. D* **111** 084054
[58] Meng Y, Wang X J, Li Y Z and Kuang X M 2025 *Eur. Phys. J. C* **85** 627
[59] Wang X J, Meng Y, Kuang X M and Liao K 2024 *Eur. Phys. J. C* **84** 1243
[60] Kuang X M, Meng Y, Papantonopoulos E and Wang X J 2024 *Phys. Rev. D* **110** L061503
[61] Porth O, Mizuno Y, Younsi Z, *et al.* 2019 *Astrophys. J. Suppl.* **243** 26
[62] Zeng X X, Zhang H Q and Zhang H 2020 *Eur. Phys. J. C* **80** 872
[63] Heydari-Fard M, Heydari-Fard M and Riazi N 2023 *Int. J. Mod. Phys. D* **32** 2350088
[64] He K J, Tan S C and Li G P 2022 *Eur. Phys. J. C* **82** 81
[65] Gao X J, Sui T T, Zeng X X, An Y S and Hu Y P 2023 *Eur. Phys. J. C* **83** 1052
[66] He K J, Guo S, Tan S C and Li G P 2022 *Chin. Phys. C* **46** 085106
[67] Wang H M, Lin Z C and Wei S W 2022 *Nucl. Phys. B* **985** 116026
[68] Yang C Y, Aslam M I, Zeng X X and Saleem R 2025 *J. High Energy Astrophys.* **46** 100345
[69] He K J, Yao J T, Zhang X and Li X 2024 *Phys. Rev. D* **109** 064049
[70] Zeng X X, Ye H, He K J and Yu H 2025 *Eur. Phys. J. C* **85** 1211
[71] He K J, Li G P, Yang C Y and Zeng X X 2025 *JCAP* **10** 003
[72] Bardeen J M 1968 *Proc. Int. Conf. GR5* (Tbilisi) pp. 174
[73] Ayon-Beato E and Garcia A 1998 *Phys. Rev. Lett.* **80** 5056
[74] Ayon-Beato E and Garcia A 1999 *Gen. Relativ. Gravit.* **31** 629
[75] Ayon-Beato E and Garcia A 1999 *Phys. Lett. B* **464** 25
[76] Ayon-Beato E and Garcia A 2000 *Phys. Lett. B* **493** 149
[77] Hayward S A 2006 *Phys. Rev. Lett.* **96** 031103
[78] Fan Z Y 2017 *Eur. Phys. J. C* **77** 266
[79] Hu Z, Zhong Z, Li P C, Guo M and Chen B 2021 *Phys. Rev. D* **103** 044057
[80] Wang K, Feng C J and Wang T 2024 *Eur. Phys. J. C* **84** 457
[81] Gralla S E, Lupsasca A and Marrone D P 2020 *Phys. Rev. D* **102** 124004